# Different routes to chaos in the Ti:sapphire laser

Marcelo G. Kovalsky and Alejandro A. Hnilo*

*Centro de Investigaciones en Laseres y Aplicaciones (CEILAP), Instituto de Investigaciones Científicas y Técnicas de las Fuerzas Armadas (CITEFA), Consejo Nacional de Investigaciones Científicas y Técnicas (CONICET), Universidad Nacional de San Martín (UNSAM), San Martín, Argentina*

(Received 23 February 2004; revised manuscript received 1 July 2004; published 19 October 2004)

Kerr-lens mode-locked, femtosecond Ti:sapphire lasers can operate in two coexistent pulsed modes of operation, named $P1$ (transform limited output pulses) and $P2$ (chirped output pulses). We study, both theoretically and experimentally, the transition to chaotic behavior for each of these two modes of operation as the net intracavity group velocity dispersion parameter approaches to zero. We find that $P1$ reaches chaos through a quasiperiodic route, while $P2$ does it through intermittency. The modulation frequencies involved, the size of the transition regions in the parameter's space, and the embedding and correlation dimensions of the attractors (and also the kurtosis for the intermittent regime) are theoretically predicted and also measured, showing a satisfactory agreement. We consider that this finding of a low-dimensional system of widespread practical use with (at least) two coexistent chaotic scenarios will have a broad impact on the studies on nonlinear dynamics.

DOI: 10.1103/PhysRevA.70.043813 PACS number(s): 42.65.Re, 42.65.Sf

## I. INTRODUCTION

The Kerr-lens mode-locked (KLM) Ti:sapphire laser is the most widespread source of femtosecond (fs) laser pulses nowadays, and it is becoming increasingly important for many applications. Yet because of the complex interlacing between spatial and temporal variables intrinsic in the KLM, it displays a variety of dynamical effects, such as period doubling and tripling [1–3], multistability [4], self $Q$ switching [5,6], and even deterministic chaos [6–9]. Many of the features of these effects are still poorly known. Their study has revealed the KLM lasers to be not only interesting because of their practical applications, but also fruitful as model nonlinear systems.

A particularly difficult challenge is the description of chaotic dynamics. The obtained signals are apparently random, so that a direct comparison between the theoretical descriptions and the experimental results is meaningless. The reason is that, in a chaotic state, any small difference between the initial conditions (say, the assumed and the actual ones) is amplified exponentially with time. At first sight, trying to grasp information from chaotic signals is as hopeless as trying to do it from "noise." However, a system in a truly deterministic chaotic state evolves in phase space following the paths of a bunch of (infinite) unstable orbits, tightly packed in a topologically complex but low-dimensional manifold usually called a *strange attractor*. "Noise," instead, comes from the coupling to the environment, which has a very large number of dynamical dimensions. From these considerations, it is clear that any study of the chaotic state must not involve a direct comparison between simulated and observed mode-locking signals, but instead the comparison (between prediction and observation) of the properties of the underlying attractor. These properties can be extracted from a numerical analysis of the time series. However, in the case of KLM lasers, the very short duration of the pulses (beyond the resolution of the fastest electronics), the high repetition rate (about 100 MHz), and the high level of noise make the recording of useful time series difficult.

To our knowledge, the first successful measurement of the features of a chaotic attractor in a Ti:sapphire KLM laser was performed by Bolton and Acton [10] through the numerical analysis of time series, of the instrumental response of photodiodes to the mode-locking signal, recorded in a large-memory digital oscilloscope. In this way, only the dynamics of the total energy of the pulses was observed, but that proved to be sufficient. A quasiperiodic route to chaos was revealed, and the correlation dimension of the attractor (which is presumably a fractal) was measured between 3 and 4. The results agreed well with the calculations of a theoretical model using iterative maps built from Gaussian matrices, which has become a standard approach to describe KLM dynamics [11,12].

The description of a nonlinear system with maps is an alternative to that with a differential equation, and no information is gained or lost. There are some immediate advantages: the dimensionality of the problem is reduced, and the numerical simulations are easier and run faster. In the particular case of KLM, additional advantages are that the stability of the solutions is easily determined and that large pulse-to-pulse variations (which are, indeed, observed in the practice) can be described without restrictions.

In general, writing the map equation can be as difficult as solving the differential equation, unless the physical system has some "internal clock" that determines the position of the adequate discrete times. In the case of KLM lasers, that clock is provided by the cavity round-trip time, whose duration is not affected by the laser dynamics. The fluctuations of the cavity round-trip time, which are due to thermal or mechanical noise, are negligible during the recording time of a time series.

In this paper, we extend the study of the chaotic dynamics in the KLM Ti:sapphire laser to include the two observable

*Permanent address: CEILAP, Zufriategui 4380, (1603) Villa Martelli, Argentina. Electronic address: ahnilo@citefa.gov.ar

 

modes of pulsed operation—namely, $P1$ (transform limited output pulses) and $P2$ (output pulses with positive chirp) [4,7]. We experimentally find that each mode follows its own, clearly distinguishable, route to chaos: $P1$ through quasiperiodicity, $P2$ through a bifurcation cascade and intermittencies. In spite of this difference, we find that the dimensionality of both attractors in the fully developed chaotic regime is between 3 and 4. Our observations confirm the results of Ref. [10] which (it is evident now) were obtained for the mode $P1$.

We also find that our simple theoretical model, based on a five-dimensional iterative map, not only predicts the different dynamical regimes for $P1$ and $P2$ and the embedding and correlation dimensions of the attractors, but also the approximate size of the transition regions and the Fourier spectra. Taking into account the approximations involved in the model and the noisy features of the nonlinear system under study, we had expected to observe only a qualitative theoretical-experimental agreement. Nevertheless, the numerical values of most of the predictions are remarkably close to the observed ones.

In the next section, Sec. II, we briefly review the theoretical model and describe the experimental setup. In Sec. III we present the results (both theoretical and experimental) for the transition from the stable mode locking to the regime of fully developed chaos, for the two pulsed modes of operation.

## II. BACKGROUND

### A. Theoretical model

The electric field in the laser pulse is assumed to be of the form

$$E(r,t) = E_0 \exp(-ikr^2/2q)\exp(-ikt^2/2p), \tag{1}$$

where $k$ is the wave vector, $r$ is the distance from the optical axis ($z$), $t$ is the time (measured from the peak of the pulse), and the parameters $p$, $q$ are

$$\frac{1}{p} = Q - i\frac{n\lambda}{\pi\tau^2}, \tag{2}$$

$$\frac{1}{q} = \frac{n}{R} - i\frac{n\lambda}{\pi\sigma^2}, \tag{3}$$

where $\lambda$ is the central wavelength, $n$ is the index of refraction of the medium (at $\lambda$), $\tau$ is the pulse duration, $Q$ is the pulse chirp, $\sigma$ is the beam waist, and $R$ is the beam radius of curvature. These equations are written for each possible polarization and for each of the directions $(x,y)$ transversal to the optical axis. We assume, as usual, that the field is linearly polarized and that astigmatism has been compensated by the cavity design (whose details are of no interest at this point). As the pulse propagates, the $p$ and $q$ parameters change according to

$$q_{\text{out}} = (Aq_{\text{in}} + B)/(Cq_{\text{in}} + D), \tag{4}$$

$$P_{\text{out}} = (Kp_{\text{in}} + I)/(JP_{\text{in}} + L), \tag{5}$$

where $\{A,\ldots,D\}$ and $\{K,\ldots,L\}$ are the nonzero elements (in an appropriately designed cavity) of the $4\times4$ matrix that describes the pulse propagation and dispersion [13]. The form of the matrix elements $\{A,\ldots,L\}$ for the usual optical elements is well known. The matrix of propagation through a series of optical elements is simply obtained by multiplication of the elementary matrices. In the Ti:sapphire rod nonlinear effects occur whose expression in terms of matrix elements deserves some comment. In the spatial domain, the Kerr nonlinearity produces self-focusing and self-shortening effects, which are taken into account in an *ABCD* matrix of the form [14]

$$\begin{pmatrix} 1 & -\gamma d/4 \\ -\gamma/d & 1 \end{pmatrix}, \tag{6}$$

where $d$ is the Rayleigh length (in the low energy limit) at the Ti:sapphire rod and $\gamma = c_\gamma U/\tau\sigma^4$, where $U$ is the total energy of the pulse. The meaning of $c_\gamma$ is discussed below. In the time domain, the Kerr nonlinearity produces a self-phase modulation of the pulse which is taken into account in an *IKJL* matrix of the form

$$\begin{pmatrix} 1 & 0 \\ \beta & 1 \end{pmatrix}, \tag{7}$$

where $\beta = c_\beta U/\tau^3\sigma^2$. The exact expression of $c_\gamma$ and $c_\beta$ are not trivial [15]. For our purposes here, we can consider them simply as constants proportional to the nonlinear Kerr coefficient $n_2$. That is why we call them "nonlinearities." They hold to $\gamma$, $\beta\delta \ll 1$, where $\delta$ is the absolute value of the net amount of (negative) group velocity dispersion (GVD) per round trip in the laser cavity. The approximations implicit in this approach are generally valid for pulses longer than 10 fs and for paraxial beams.

It is convenient to define new pulse variables $S = 1/\sigma^2$, $T = 1/\tau^2$, and $\rho = 1/R$. The expressions that link the variable values at the exit rod surface (i.e., propagating towards the output mirror; see Fig. 1) at the $(n+1)$ round trip in the laser cavity with the ones at the $n$ round trip are then

$$S_{n+1} = \frac{S_n}{(\mathbf{A} + \mathbf{B}\rho_n)^2 + (\mathbf{B}\lambda S_n)^2}, \tag{8}$$

$$\rho_{n+1} = \frac{(\mathbf{A} + \mathbf{B}\rho_n)(\mathbf{C} + \mathbf{D}\rho_n) + \mathbf{BD}(\lambda S_n)^2}{(\mathbf{A} + \mathbf{B}\rho_n)^2 + (\mathbf{B}\lambda S_n)^2}, \tag{9}$$

$$T_{n+1} = \frac{T_n}{(\mathbf{K} + \mathbf{I}Q_n)^2 + (\mathbf{I}T_n/\pi)^2} = T_n\frac{\mathbf{L} - \mathbf{I}Q_{n+1}}{\mathbf{K} + \mathbf{I}Q_n}, \tag{10}$$

$$Q_{n+1} = \frac{(\mathbf{K} + \mathbf{I}Q_n)(\mathbf{J} + \mathbf{L}Q_n) + \mathbf{IL}(T_n/\pi)^2}{(\mathbf{K} + \mathbf{I}Q_n)^2 + (\mathbf{I}T_n/\pi)^2}, \tag{11}$$

where $\{A,\ldots,D\}$ and $\{K,\ldots,L\}$ are the elements of the corresponding round-trip matrices. The equation for the variable "pulse energy" $U$ has several possible forms. For example, a sixth variable for the population inversion can be introduced, and then the equation for $U$ is obtained in a straightforward

way. Nevertheless, we have found that if self $Q$ switching is not present (and this can be the case even well inside the chaotic region), then the approximation

$$U_{n+1} = U_n\left\{1 - \frac{2}{\mu}\left(\frac{U^* S_n + U_n S^*}{D_s}\right) + 4\frac{\mu - 1}{\mu}\right\} \quad (12)$$

is sufficient for our purposes. Equation (12) is obtained by expansion of the usual expression for gain saturation for the mean values $U^*$ and $S^*$, $D_s$ is the saturation energy flux for Ti:sapphire (i.e., the saturation energy multiplied by the cavity round trip time), and $\mu$ is the product of the small signal gain and the single-passage feedback factor due to linear losses (mirror reflectivity, scattering, misalignment, etc.).

The matrix elements in Eqs. (8)–(11) include the nonlinearities $\{\gamma, \beta\}$, calculated when the pulse propagates towards the output mirror (see Fig. 1), and also the nonlinearities $\{\gamma', \beta'\}$, calculated when the pulse returns from the output mirror. The general form of the *ABCD* matrix elements is then

$$A = A_0 + \gamma A_\gamma + \gamma' A_{\gamma'} + [\text{higher orders in } n_2 \text{ (neglected)}] \quad (13)$$

(the same for $B$, $C$, $D$), where the coefficients are algebraically intricate functions of the geometrical parameters of the cavity. The *KIJL* matrix elements are simpler (at first order in $n_2$):

$$K = 1 + 2\delta\beta',$$

$$I = 2\delta,$$

$$J = 2\delta\beta\beta' + \beta + \beta',$$

$$L = 1 + 2\delta\beta. \quad (14)$$

The recursive relations (8)–(14) form the simplest iterative map that appropriately describes the KLM laser dynamics. But even this highly simplified five-dimensional description is excessive, for even the most complex dynamics of this system evolve, as we will see, inside a four-dimensional space.

The laser operation values are obtained by imposing that the variables at the $(n+1)$ round trip be equal to the ones at the $n$ round trip. These are the fixed points of the map, which show very good agreement with the observed stable pulse values [12]. The fixed points can be obtained easily from Eqs. (10) and (11). An immediate solution is $T_n = T_{n+1} = 0$. This corresponds to a continuous-wave solution (pulse duration $\tau \to \infty$), which is named $P0$. If $T \neq 0$, then there is one solution with $Q_n = Q_{n+1} = Q^* = 0$ (transform-limited pulse), which implies $K = L$ and hence $\beta \approx \beta'$; that is, the magnitudes of the nonlinearities are the same for both directions of propagation. This solution is named $P1$, and it corresponds to the shortest observable pulses. Another solution is obtained assuming that $Q^* \neq 0$; then, $2IQ^* = L - K$ and $Q^* = \beta\text{-}\beta'$. In turn, this solution splits into two: one in which the "backwards" nonlinearity $\beta'$ is negligible, and hence pulses with positive chirp are obtained at the output mirror (named $P2$), and the opposite case, which corresponds to output pulses with negative chirp (named $P3$). These solutions have a simple interpretation also in physical terms [4].

The stability of the solutions is easily obtained by calculating the eigenvalues of the round-trip matrices at the fixed points. If for a given set of the parameter values one of the eigenvalues becomes larger than 1 (in modulus), then the solution becomes unstable, and the corresponding eigenvector indicates the direction (in phase space) of this instability. The way the eigenvalue crosses the circle of radius 1 (in the complex plane) also gives us some information. For example, if it does it by becoming smaller than $\sim 1$, we expect to see an instability by period doubling (and this is, indeed, what is experimentally observed). This analysis also explains why the solution $P2$ is more robust than the $P1$ (even though both coexist in a large volume of the parameter space) and why the $P3$ solution has never been observed [4].

In order to describe the dynamics in the unstable regime, we choose as the initial condition a perturbation of the fixed point, and then the complete map (8)–(14) is numerically iterated. The time series of one or several of the pulse variables are stored after a transient (typically $10^4$ iterations, which corresponds to $\approx 100$ $\mu$s in real time). In what follows, the length of these numerically generated series is chosen to be comparable to that of the experimentally obtained ones (about 2200 iterations; see below). In this way, any difference between the prediction and the observation is known to be caused by experimental imperfections or to failures of the model, but not to numerical artifacts. The only exceptions to this criterion are the series used for drawing the attractors (Figs. 8 and 10), which are significantly longer than the experimental ones, because short series produce blurred figures. These exceptions are justified, for these figures have only illustrative purposes.

The parameters in these simulations are taken from measured or tabulated values. They are summarized in the Appendix. No numerical fine-tuning of the parameters is performed. As was commented on before, we cannot expect a precise reproduction of the experimental time series because of the extreme sensitivity to perturbations characteristic of nonlinear systems. That is, looking for a precise numerical concordance is meaningless. So we limit ourselves to a comparison of the properties of the observed and the predicted attractors and, even in this case, we expect a qualitative rather than a quantitative agreement. Despite this and as is shown below, often the numerical agreement reached is surprisingly good.

### B. Experimental setup

A scheme of our Ti:sapphire laser is shown in Fig. 1. It is constructed in the $X$ configuration, with a flat HR rear mirror ($M_4$) and a 12% output coupler ($M_1$). The total cavity length is 1724 mm (mode-locking rate or cavity frequency: 86.94 MHz), and the typical output power is 0.4 W for 5 W of continuous-wave pumping at 532 nm. The typical spectral bandwidth of the output is 30 nm, centered at 820 nm. A typical pulse duration for stable mode locking is 35 fs (transform limited, mode $P1$) or 65 fs (chirped, mode $P2$).

To obtain the experimental time series, we essentially follow the experimental approach of Ref. [10]. We measure the

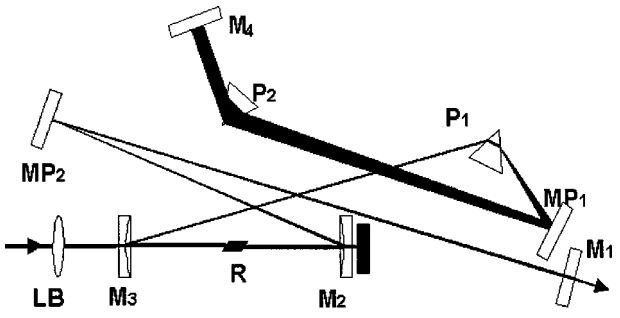


FIG. 1. Scheme of our Ti:sapphire laser. LB, pump focusing lens ($f$=10 cm); $M_{2,3}$, curved mirrors (radius, 10 cm); $R$, laser rod (length, 4 mm); $MP_{1,2}$, plane mirrors; $P_{1,2}$, pair of fused silica prisms introducing negative GVD. Distances in mm: $M_3-R=R-M_2$, 50; $M_2-MP_2$, 140; $MP_2-M_1$, 465; $M_3-P_1$, 297; $P_1-MP_1$, 198; $MP_1-P_2$, 415; $P_2-M_4$, 109.

pulse train with a fast response (0.5 ns rise time) photodiode and store the output, in the single-sweep mode, in a large-memory (50 K samples, 8 bits in single sweep mode), high-speed (2 G samples/s) digital oscilloscope. We use a small area photodiode (0.2 mm diameter), displaced from the center of the relatively large laser beam (size 2.5 mm diameter at the point of observation). In this way, we expect to detect variations not only in the pulse energy, but also variations in the beam area. According to the theoretical predictions and our previous observations, the beam area is the variable that becomes unstable most easily, so that it is, *prima facie*, the most convenient one to unfold the dynamics.

The photodiode is too slow to resolve the fs pulse shape. What we observe is the instrumental response to the fs pulse. The valuable information is contained in the observed pulse peak value, which is proportional to the pulse energy collected by the photodiode. We record 50 000 sample points separated 0.5 ns, which cover a series of roughly 2200 successive mode-locking pulses. As an illustration, a section of an experimental time series is shown in Fig. 2 (a complete time series produces a blurred figure).

On the average, there are 23 points to determine the shape of the signal during a round-trip time, but the main part of these points just draws the base line between successive

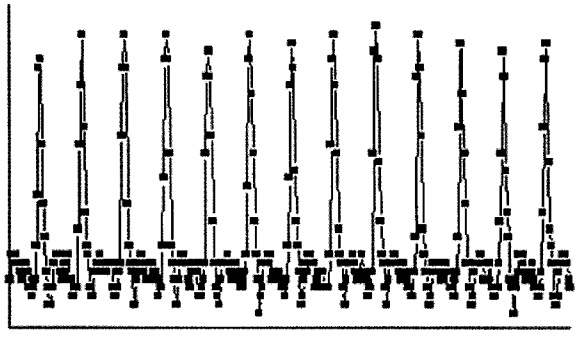

FIG. 2. A section (about 3400 points or 150 ns) of a typical experimental time series obtained as explained in the text. Note that the complete experimental time series is much longer (50 000 points or 25 $\mu$s). Lines are added to the sample points to make the pulses easier to see.

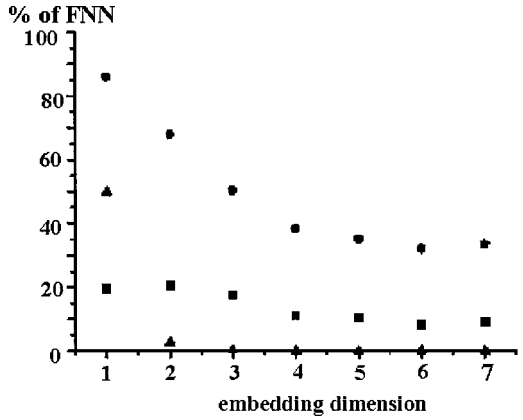


FIG. 3. The percentage of false nearest neighbors (FNN's) as a function of the embedding dimension, for the three methods of obtaining a processed time series from the same experimentally obtained time series (partially displayed in Fig. 2). The area and raw-peak methods produce processed time series with a high level of contamination with noise. The polynomial-fitting method produces an acceptable, low-noise time series. Squares: raw peak method. Circles: area method. Triangles: polynomial method.

mode-locking pulses and is almost useless. Only a few points are available to draw each peak. Of course, seldom does a sample point coincide with the real peak of the pulse. In order to find the value of the real peak of the pulse, we essayed three different methods to reconstruct the original (instrumental response) pulse. One method (following Ref. [10]) is to use a fourth-order polynomial algorithm to find the best fitting to the ten points closest to the peak. Then, the value of the maximum of the fitting curve is taken as the value of the real peak of the (instrumental response) pulse. A second method is to fit with a (instrumental response-shaped) pulse with the same area than the area below the sample points. Finally, the third method is simply to pick up the highest sample point in each round trip. For a given experimental run, each method produces slightly different "processed" time series.

To evaluate which one of the three methods provides the series with the lowest noise, we compute the number of false nearest neighbors (FNN's) [16] as a function of the embedding dimension ($d_E$) in each "processed" time series for all the experimental series available. To do this we use the method by Kennel *et al.* [17]. A number of FNN's falling to zero (and staying equal to zero) as $d_E$ increases is considered a good indicator of a noise-free time series. In Fig. 3 we show a typical result, obtained from the complete time series of Fig. 2.

The raw-peak method gives an erratic behavior of the number of FNN's, never reaching zero. The area method appears to reach a stationary value of 35% (the raw time series displays a pulse to pulse variation of only about 10%), but then it increases again, indicating a high level of contamination with noise. Finally, the polynomial method decays to zero for a dimension of 3 and stays there, being, in consequence, the best of the three. As a further check, we computed the percentage of FNN's for the polynomial method processed series with surrogate data [16], obtaining a

near-constant value around 50%, regardless of the value of $d_E$. This indicates that the polynomial-method-processed series does contain dynamical information, which is lost when the data are "scrambled."

In summary, for all the experimentally obtained series the polynomial method (originally proposed in Ref. [10]) produced the best noise-free processed series. In what follows, all the results presented, are obtained from polynomial-method-processed series.

The laser normally operates in a region where modes $P1$ and $P2$ coexist. Mechanical perturbations induce spontaneous transitions from one of the modes to the other. They can be recognized by observation of the spectrum (bell shaped for $P1$, square edged for $P2$), the pulse duration (almost twice longer for $P2$ than for $P1$), and by eye, as a slight variation of the spot size. By displacing the prisms (see Fig. 1) the amount of glass inside the laser cavity is increased, so that the net value of the GVD approaches zero (from the negative side) without affecting the laser alignment. The pulse duration shortens (the mode $P2$ twice as fast as the mode $P1$) until the mode-locking train becomes unstable. The fluctuations are moderate at first, but as the value of the net GVD goes closer to zero, they become wild and unpredictable, apparently chaotic. In the next section, we show how this process develops in a different way for each of the modes $P1$ and $P2$ and that the fully developed instability is not mere noise, but deterministic, low-dimensional chaos.

## III. RESULTS

### A. Embedding dimension

The observed dynamical regimes have their corresponding representation, in phase space, as manifolds of different dimension. Perfect mode locking corresponds to a single point (dimension=zero), period doubling to two separate points (two manifolds of zero dimension), periodic oscillations with a single frequency to a closed curve (dimension =1), periodic oscillations with two incommensurate frequencies to a torus (dimension=2), and deterministic chaos to a strange attractor (dimension fractal). In consequence, as the value of the GVD approaches zero and the instabilities of the mode locking become more and more complex, we expect the embedding dimension ($d_E$) of the time series to increase. However, even in the fully developed chaotic regime we also expect $d_E$ to remain a small number, because a high embedding dimension does not mean deterministic chaos, but just noise.

In Fig. 4, we plot the measured and predicted values of $d_E$ for the mode $P1$ as a function of the net GVD per round trip. As in Sec. II B, we find $d_E$ as the smallest dimension value at which the number of FNN's, for each time series, drops to zero (we always check that it stays equal to zero for larger dimension values).

It is very satisfactory to find that both the experimental and theoretical values saturate in the small number $d_E=4$. The numerical values of the GVD at which the transitions occur do not deserve much attention, because the measurement of the absolute value of the GVD has a large error (it involves measuring beam path lengths inside the prisms with a precision of tenths of mm). More significant is the width of the region of transition from stable mode locking to fully developed chaos. This transition for the mode $P1$ is measured to span over 40 fs$^2$, while the predicted value is 3 times larger: 130 fs$^2$. This difference is explained by the presence (in the real laser, but not in the simulations) of the competing mode $P2$, which is more stable than $P1$ and therefore tends to shrink the operable region of $P1$. An additional element of perturbation is the impossibility to obtain stable mode locking for GVD values at the left of about $-110$ fs$^2$, for the beam touches the edge of the prism and coupling to transversal modes appears. These effects are not present regarding the transitions of $P2$ (Fig. 5: note that it occurs for higher values of the GVD) and, indeed, the width of the predicted (12 fs$^2$) and measured (11 fs$^2$) transitions show excellent agreement in this case. As in the case of $P1$, the maximum value reached by $d_E$ is 4. We remark that the series of surrogate data (for both modes and all values of GVD) do not provide a definite value for $d_E$.

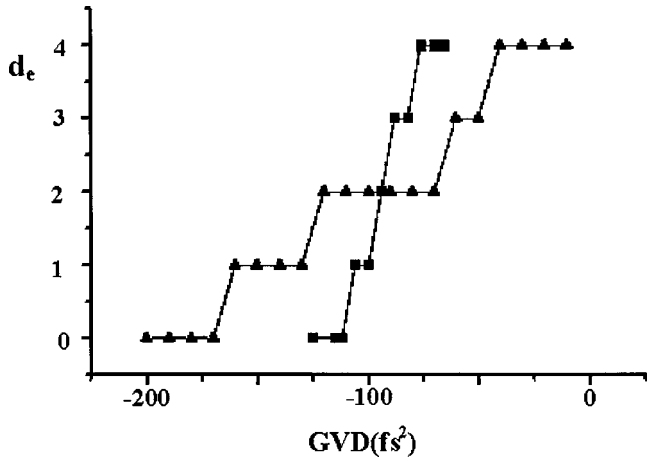


FIG. 4. Embedding dimension for the dynamics of the mode $P1$ as function of GVD. Squares: experimental data. Triangles: numerically obtained data.

### B. Correlation dimension

As already stated, in the region close to zero GVD the mode-locking train shows unpredictable fluctuations. The

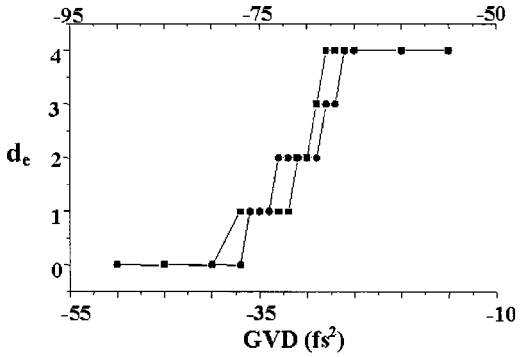


FIG. 5. Embedding dimension for the dynamics of the mode $P2$ as function of GVD. Upper axis: value of GVD for the experimental data (squares), lower axis, for the numerically obtained data (circles).

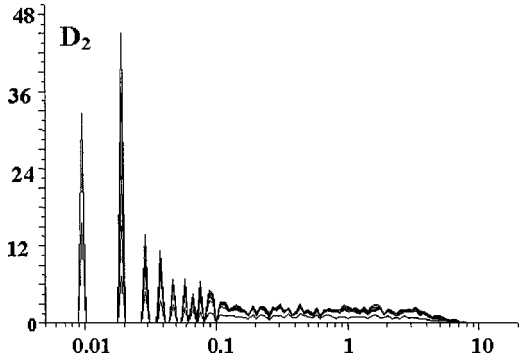


FIG. 6. Correlation dimension for the mode $P1$ (from experimental data, GVD$=-29$ fs$^2$). Curves for increasing values of the embedding dimension are plotted. Note the plateau more than one decade wide.

Fourier spectra are wide and noisy (see also Secs. III C and III D). The low value of the embedding dimension indicates that the unpredictability is caused by the complex underlying dynamics. But the mark of chaotic dynamics is the presence of a strange attractor, identified by a noninteger, or fractal, correlation dimension ($D_2$). As the algorithms to calculate the correlation dimension are very sensitive to noise, they provide an additional check of the reliability of the time series.

We use the customary algorithm by Grassberger and Procaccia. For the mode $P1$ and GVD of $-29$ fs$^2$ the (experimental) time series is apparently chaotic. In Fig. 6 we plot the calculus of $D_2$ for increasing embedding dimensions. The plateau in $\log(l)$ more than one decade wide indicates a deterministic behavior and also that the time series are sufficiently noise free.

For the numerical evaluation of $D_2$, instead, we plot it versus the embedding dimension [Fig. 7(a)]. It is clearly seen that the correlation dimension lies between 3 and 4. The theoretical prediction (from time series obtained from the numerical iteration of Eqs. (8)–(14)) is coincident. The numerically generated series display a fractal correlation dimension for a wide range of values of GVD. The experimental ones showing a fractal dimension, instead, are restricted to a region 5 fs$^2$ wide (for the mode $P1$). Beyond this region the laser easily collapses to mode locking and $Q$ switching, and the data are not reliable any longer.

For the mode $P2$ we apply the same method, starting at $-25$ fs$^2$. As the whole transition from stable mode locking to fully chaotic dynamics occurs here in only 11 fs$^2$, the process of data recording is still more difficult than for $P1$, which is reflected in larger error bars. Anyway, from the plot of $D_2$ vs $d_E$ [Fig. 7(b)] we conclude again that the fractal dimension is between 3 and 4, and that the agreement between our model and the experimental results is satisfactory.

The same procedure carried out with surrogate data produces always increasing values of $D_2$ vs $d_E$ both for $P1$ and $P2$.

### C. Route to chaos of mode *P*1 (quasiperiodicity)

We have verified that the dynamics near the zero GVD point is truly chaotic and that the correlation dimensions of

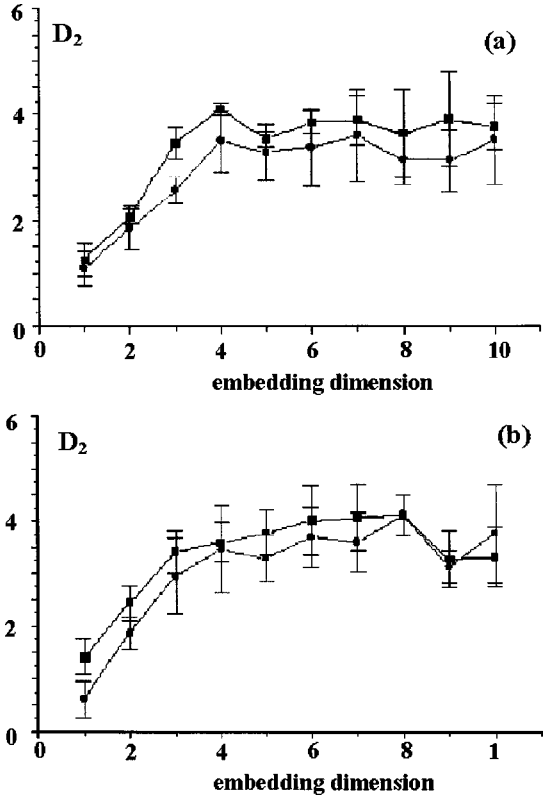


FIG. 7. Correlation dimension of the chaotic attractors of the modes $P1$ (a) and $P2$ (b). Each point in these plots is calculated from the plateaus of $D_2(l,m)$ as a function of $\log(l)$ (see Fig. 6). For both modes the correlation dimension (both the theoretical and the experimental) is between 3 and 4, an indication of low-dimensional chaos. Squares: from experimentally obtained time series. Triangles: from numerically generated time series.

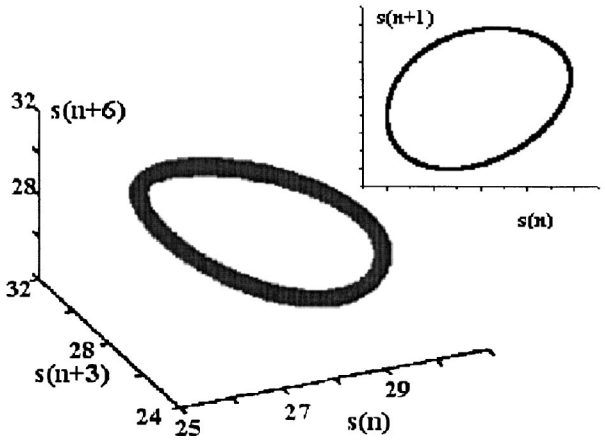


FIG. 8. Three-dimensional representation of the (numerically obtained) toroidal attractor underlying $P1$ at GVD$=-55$ fs$^2$ ($d_E=3$)—i.e., just before the onset of the chaotic instability. Note that the time lag is 3, which corresponds to the first minimum of the average mutual information. This drawing is made of $10^4$ iterations after leaving out a transient of 5000. The inset displays a first return map for the same time series and shows the section of the torus. Compare the differences with the attractor of $P2$ in the same dynamical situation (Fig. 10).

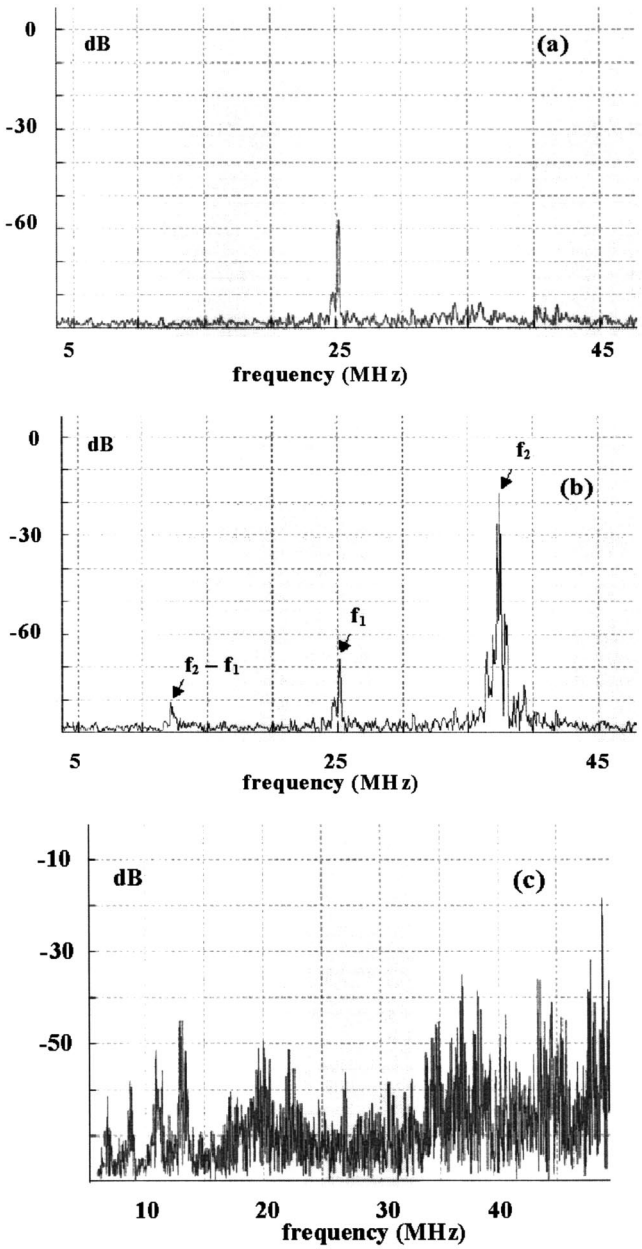


FIG. 9. Experimentally obtained Fourier spectra of the mode $P1$ for different dynamical situations: (a) the first oscillation shows up at 25.0 MHz (GVD=−96 fs$^2$), (b) a second frequency at 37.4 MHz appears, and also a beating at 12.4 MHz (GVD=−90 fs$^2$), and (c) well inside the chaotic region (GVD=−74 fs$^2$). Compare with the chaotic spectrum for the mode $P2$ in Fig. 11(c).

the strange attractors are between 3 and 4 for both modes $P1$ and $P2$. Nevertheless, the *scenarios*, or *routes*, that each mode follows to reach the chaotic state are different. In this paragraph we show that the mode $P1$ follows a quasiperiodic route to chaos. Hence we confirm the results obtained in the Ref. [10].

We make use of the results of the "embedding theorem" [16], which says (roughly speaking) that in a nonlinear system the structure of the underlying attractor can be revealed, or unfolded (no matter what is the original phase space), in a vector space of dimension $d_E$ reconstructed from a series of

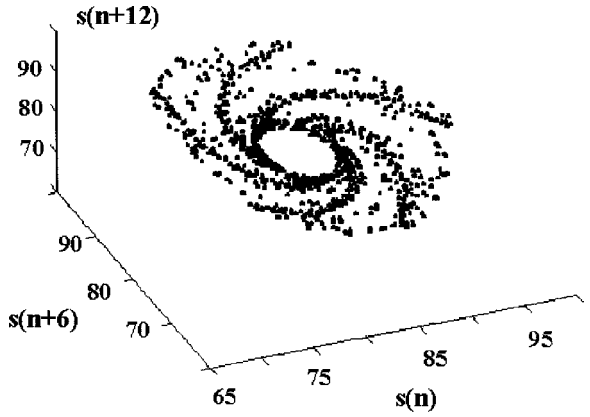


FIG. 10. Three-dimensional representation of the (numerically obtained) attractor underlying $P2$ at GVD=−27 fs$^2$ ($d_E$=3) just before the onset of the chaotic instability. Note that the time lag is 6, which corresponds to the first minimum of the average mutual information. This drawing is made of $10^4$ iterations after leaving out a transient of 5000. Compare the differences with the attractor of $P1$ at the same dynamical situation (Fig. 8).

scalar measurements. If the scalar time series is of the form of equally spaced measurements $\{s(1),s(2),\ldots,s(N)\}$ (which is precisely what we have), then the attractor can be reconstructed by building vectors $\{(s(n),s(n+m),s(n+2m),\ldots,s(n+(d_E-1)m))\}$. The value of the time lag $m$ is a central issue in this reconstruction. We follow Abarbanel's prescription [16] and choose $m$ as the first minimum in the average mutual information versus time delay of the time series. This number results in being 3 for the mode $P1$ in both the experimental and the theoretical time series.

The reconstructed attractor for a GVD value just before the chaotic region (which implies $d_E$=3; see Fig. 4) is shown in Fig. 8 for a numerically generated series. The shape of the torus and the circular shape of its section are clearly seen, an indication of the existence of two incommensurate frequencies or quasiperiodicity.

In Fig. 9, we display some experimentally obtained Fourier spectra as the GVD increases, to illustrate the transition to chaos. At −96 fs$^2$ a first oscillation of the mode locking train appears at 25.0 MHz [Fig. 9(a)]. At −90 fs$^2$ a second, incommensurate frequency appears at 37.4 MHz [Fig. 9(b), also a small beating note at 12.4 MHz]. The spectrum becomes wide, apparently chaotic, at about −74 fs$^2$ [Fig. 9(c)]. The numerically generated series show a remarkable agreement in the values of the involved frequencies: the first oscillation peak lies at 22.46 MHz and the second one at 33.39 MHz.

In comparison with the analogous experiment reported in Ref. [10], the two frequencies involved are in the range of the tens of MHz in our case, while in that experiment they were very different from each other (i.e., 2 and 30 MHz). We do not observe the period-3 subharmonic oscillation (it should appear at 86.94/3=28.98 MHz in our case) which was observed in Ref. [10]. The origin of this oscillation was hypothesized to be the beating with spatial transversal modes. With respect to this, we can say that we take special care, at each step in the experiment, to ensure a single-

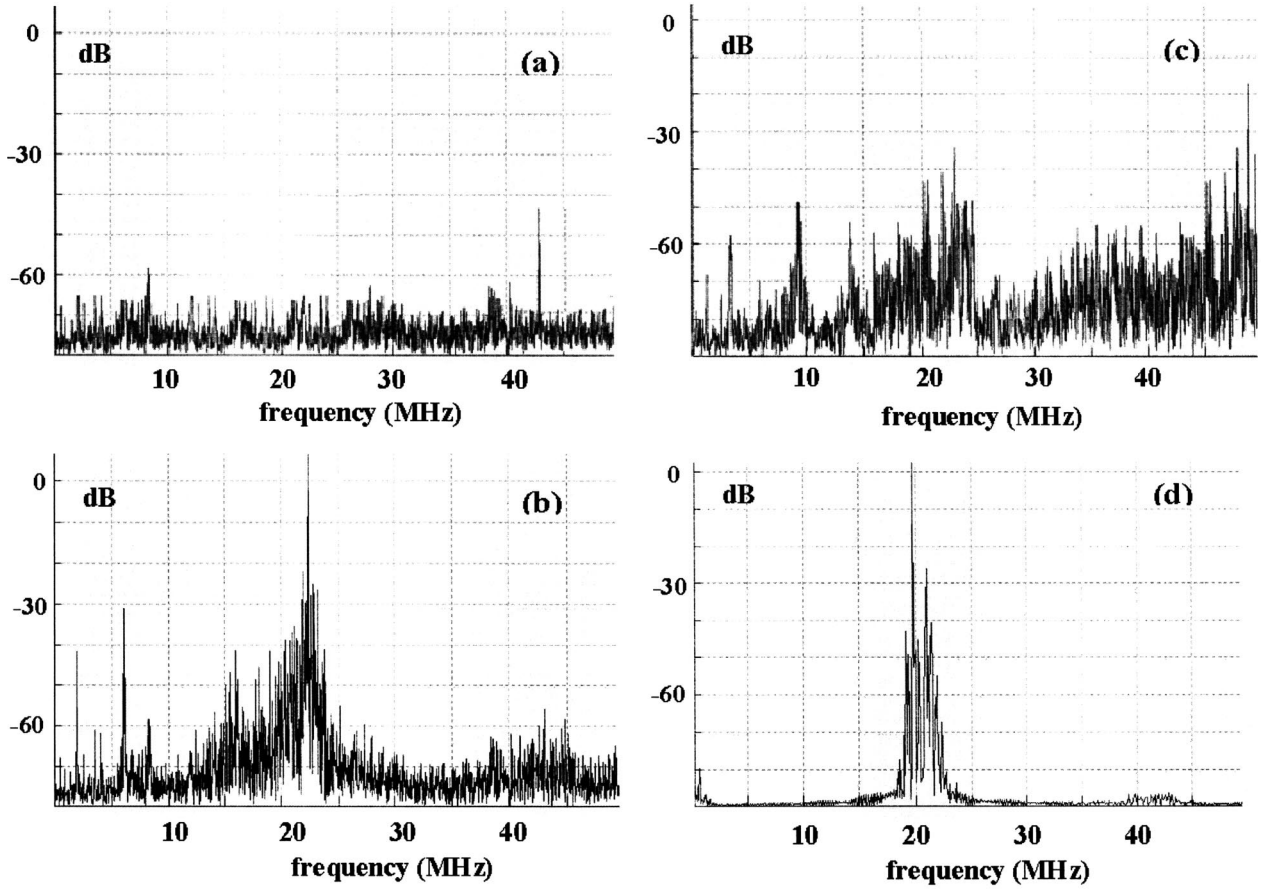


FIG. 11. Experimentally obtained [except for (d)] Fourier spectra of the mode $P2$ for different dynamical situations: (a) a first bifurcation of the cavity frequency shows up (GVD$=-76$ fs$^2$), (b) a second bifurcation occurs and both peaks broaden at the onset of chaos (GVD$=-69$ fs$^2$), and (c) inside the chaotic region (GVD$=-64.94$ fs$^2$). Compare with the chaotic spectrum for the mode $P1$ in Fig. 9(c). (d) Spectrum of a numerically obtained time series, just before the onset of chaos. Compare the similarities with the experimental spectrum at the same dynamical situation (b).

transversal-mode oscillation. This is a plausible reason for this difference between the observations. However, as the authors of Ref. [10] reported that the mode remained Gaussian all throughout the transition to chaos, it should not be discarded that the cause of the difference is simply in the details of the experimental setups. Nevertheless, both experiments coincide in the existence of a quasiperiodic route to chaos for the transform limited pulse mode (or $P1$ in our notation) and a chaotic attractor with a correlation dimension between 3 and 4. As was stated before, these are the only kind of results that one can reasonably expect to be confirmed (or refuted) by independent experiments performed on different setups for a highly nonlinear and noisy system such as the KLM Ti:sapphire laser.

#### D. Route to chaos of mode *P*2 (intermittency)

For mode $P2$, the first minimum in the average mutual information versus time delay of the time series is 6, in both the experimental and the theoretical series. As in Sec. III C, we use time series corresponding to a value of GVD just before the chaotic region ($d_E=3$), so that a three-dimensional drawing has sense. In Fig. 10, a numerically generated series is used to reconstruct the shape of the attractor, which has an appearance clearly different from that of $P1$. It seems to have a central "ring" and a region scattered outwards. This outer region is the one "explored" during the sudden excursions made by the system (see below).

In Fig. 11, we display some experimental Fourier spectra for the mode $P2$. At about $-76$ fs$^2$ a $f/2$ bifurcation occurs [a frequency peak at 43.47 MHz, Fig. 11(a)]. As GVD increases, a second bifurcation occurs (21.73 MHz) and both peaks broaden [Fig. 11(b)]. Well inside the chaotic region [GVD$=-64.94$ fs$^2$, Fig. 11(c)] the spectrum shows no easily recognizable features.

The numerically generated series show a coincident behavior: a first bifurcation at $-36$ fs$^2$, then a second one at $-33$ fs$^2$, and both peaks broaden, and finally the fully developed chaos. The spectrum of the numerically generated series for the regime just at the onset of chaos [Fig. 11(d)] shows a remarkable similarity with the experimentally obtained one [Fig. 11(b)].

Inside the chaotic regime, the time trace of the pulses shows a quasistable or laminar behavior, suddenly interrupted by an irregular or turbulent phase (see Fig. 12). As the GVD value is varied, the duration of the turbulent phase

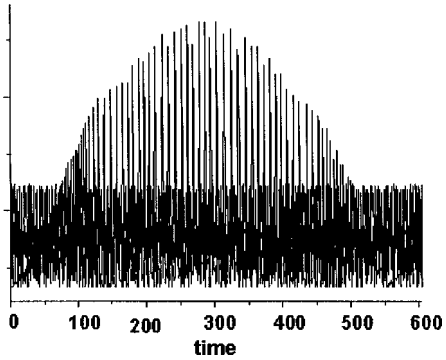


FIG. 12. Section of an experimental time series for the mode $P2$ at the onset of the chaotic region (horizontal scale, round trip time; vertical scale, arbitrary units). The pulses show a quasistable or laminar behavior, suddenly interrupted by an irregular or turbulent phase (which appear as the excursions far from the inner ring in the Fig. 10). As the GVD value is varied, the duration of the turbulent phase increases, until reaching the full developed chaos. The kurtosis of this time series (complete) is $\approx 12$.

increases, until reaching the fully developed chaos.

Based on these observations, we hypothesize that $P2$ follows a route to chaos through intermittency. Intermittency is usually quantified through the statistical quantity named *kurtosis*:

$$k = \frac{\sum_{i=1}^{n} (y_i - \overline{y})^4}{(N-1)s^4}, \tag{15}$$

where $\overline{y}$ is the average value of the time series and $s$ is its standard deviation. The kurtosis of a normal distribution is 3, so that it is usual to define the kurtosis excess as $k_e = k - 3$. In this way, a negative value of $k_e$ indicates a relatively flat distribution, while a positive value of $k_e$ indicates that the tails of the distribution have a high weight. This is a characteristic of the distributions generated by an intermittent behavior because of the large, sudden excursions from the average value.

The experimental series of $P2$ obtained for $d_E = 2$ have a very small value of $k_e$. For those with $d_E = 3$, $k_e$ is about 10, and for the series obtained inside the chaotic region ($d_E = 4$), $k_e$ reaches values close to 1000. The same happens for the numerically generated time series. From all this experimental and theoretical evidence, we conclude that $P2$ evolves to chaos following a particular route, showing first a bifurcation cascade and then intermittencies.

## IV. CONCLUSIONS

In this paper, we have shown, both theoretically and experimentally, that the two observable pulsed solutions in the KLM Ti:sapphire laser—namely, $P1$ (transform limited output pulses) and $P2$ (chirped output pulses) evolve to a low-dimensional chaotic state by following their own route to chaos: $P1$ through quasiperiodicity, $P2$ through period doubling and intermittency. Besides, we have been able to measure the fractal dimension of the chaotic attractors, which are both between 3 and 4. We note that the attractors are different, the dynamics of $P1$ and $P2$ being easily distinguishable, even at the threshold of the chaotic region, by their Fourier spectra. We believe that this finding—i.e., a low-dimensional system of practical importance which spontaneously presents the coexistence of (at least) two chaotic scenarios—will have a great impact on the studies on nonlinear dynamics.

The good agreement obtained between the predicted and the measured properties, all along the transition to chaos, means an additional support to our already tested simplified description with a five-dimensional iterative map. In particular, the model is able to predict the appearance of the frequencies in the quasiperiodic regime of the mode $P1$, without assuming the oscillation of transversal modes. For the mode $P2$, the bifurcation cascade and the peak broadening before entering the chaotic regime are also correctly predicted. Taken into account that the model is quite schematic and the characteristics of the nonlinear system under study, we had expected to observe only a qualitative theoretical-experimental agreement. However, the quantitative agreement obtained in many cases is remarkable.

There are still many issues to advance in the study of this system. To mention just a few: to find the best set of four variables to describe the chaotic dynamics, to draw sections of the chaotic attractors, to look for trajectories linking the two chaotic attractors, and to identify the catastrophes of the Lyapunov surface leading to the mode locking instabilities. Nevertheless, we have found appealing the application to the design of a simple scheme of control of chaos [18], because of its practical consequences. We have calculated that, by stabilizing the mode locking inside the chaotic region by adjusting the cavity losses, pulses 2 times shorter than in the limit of the normally stable region may be attained [19].

## ACKNOWLEDGMENTS

Many thanks to Dr. Mario Marconi for his hospitality in the *Laboratorio de Electrónica Cuántica* (*Universidad de Buenos Aires*), where the experimental part of this work was carried out, and to Dr. Francisco Manzano (CEILAP) for lending the large memory oscilloscope. This work received support from the subsidies CONICET PIP 0425/98 and 0639/98, and from Contract No. PICT99 03-06303 of the *Agencia Nacional de Promoción Científica y Tecnológica* (ANPCYT).

## APPENDIX: NUMERICAL VALUES OF THE PARAMETERS USED IN THE SIMULATIONS

The geometrical parameters are indicated in the caption of the Fig. 1 and lead to the following values of the elements of the ABCD round-trip matrix: $A_0 = 4.138\,138$, $B_0 = -2.304\,786$ cm, $C_0 = 8.327\,616$ cm$^{-1}$, $D_0 = -4.3965$, $A_\gamma = 3.547\,58$, $B_\gamma = 1.315\,279$ cm, $C_\gamma = -3.246\,724$ cm$^{-1}$, $D_\gamma = 8.224\,233$, $A_{\gamma'} = 0.243\,136$, $B_{\gamma'} = -0.073\,09$ cm, $C_{\gamma'} = -4.6188$ cm$^{-1}$, and $D_{\gamma'} = 0.632\,04$.

Other parameters' values are $c_\gamma = 1.38 \times 10^{-11}$ cm$^4$ fs nJ$^{-1}$, $c_\beta = 2.18 \times 10^{-7}$ cm$^2$ fs nJ$^{-1}$, $\mu = 1.61$, and $D_s = 1.22$ mJ/cm$^2$.

[1] M. Kovalsky, A. Hnilo, and C. González, Opt. Lett. **24**, 1638 (1999).
[2] D. Cote and H.M. Van Driel, Opt. Lett. **23**, 715 (1998).
[3] S. Bolton, R. Jenks, C. Elkinton, and G. Sucha, J. Opt. Soc. Am. B **16**, 339 (1999).
[4] M. Kovalsky, A. Hnilo, A. Libertun, and M. Marconi, Opt. Commun. **192**, 333 (2001).
[5] Q. Xing, W. Zhang, and K.M. Yoo, Opt. Commun. **113**, 119 (1995).
[6] J. Jasapara, W. Rudolph, V. Kalashnikov, D. Krimer, I. Poloyko, and M. Lenzner, J. Opt. Soc. Am. B **17**, 319 (2000).
[7] M. Kovalsky and A. Hnilo, Opt. Commun. **186**, 155 (2000).
[8] I. Christov, V. Stoev, M. Murnane, and H. Kapteyn, Opt. Lett. **20**, 211 (1995).
[9] Q. Xing, L. Chai, W. Zhang, and C. Wang, Opt. Commun. **162**, 71 (1999).
[10] S. Bolton and M. Acton, Phys. Rev. A **62**, 063803 (2000).
[11] J. Chilla and O. Martínez, J. Opt. Soc. Am. B **10**, 638 (1993).
[12] A. Hnilo, J. Opt. Soc. Am. B **12**, 718 (1995).
[13] A. Kostenbauer, IEEE J. Quantum Electron. **26**, 1148 (1990).
[14] V. Magni, G. Cerullo, and S. De Silvestri, Opt. Commun. **101**, 365 (1993).
[15] M. Marioni and A. Hnilo, Opt. Commun. **147**, 89 (1998).
[16] H. Abarbanel, *Analysis of Observed Chaotic Data* (Springer-Verlag, New York, 1996).
[17] M. Kennel, R. Brown, and H. Abarbanel, Phys. Rev. A **45**, 3403 (1992).
[18] E. Ott, C. Grebogi, and J. Yorke, Phys. Rev. Lett. **64**, 1196 (1990).
[19] M. Kovalsky, Ph.D. thesis, Facultad de Ciencias Exactas, Universidad de Buenos Aires, 2004.